

A Mass Conserved Reaction–Diffusion System Captures Properties of Cell Polarity

Mikiya Otsuji^{1*}, Shuji Ishihara², Carl Co³, Kozo Kaibuchi⁴, Atsushi Mochizuki², Shinya Kuroda⁵

1 Department of Anesthesiology, Faculty of Medicine, University of Tokyo, Tokyo, Japan, **2** Division of Theoretical Biology, National Institute for Basic Biology, Okazaki, Japan, **3** Department of Cellular and Molecular Pharmacology and Program in Biological Sciences, University of California San Francisco, San Francisco, California, United States of America, **4** Department of Cell Pharmacology, Graduate School of Medicine, Nagoya University, Nagoya, Japan, **5** Department of Biophysics and Biochemistry, Graduate School of Science, University of Tokyo, Tokyo, Japan

Cell polarity is a general cellular process that can be seen in various cell types such as migrating neutrophils and *Dictyostelium* cells. The Rho small GTP(guanosine 5'-tri phosphate)ases have been shown to regulate cell polarity; however, its mechanism of emergence has yet to be clarified. We first developed a reaction–diffusion model of the Rho GTPases, which exhibits switch-like reversible response to a gradient of extracellular signals, exclusive accumulation of Cdc42 and Rac, or RhoA at the maximal or minimal intensity of the signal, respectively, and tracking of changes of a signal gradient by the polarized peak. The previous cell polarity models proposed by Subramanian and Narang show similar behaviors to our Rho GTPase model, despite the difference in molecular networks. This led us to compare these models, and we found that these models commonly share instability and a mass conservation of components. Based on these common properties, we developed conceptual models of a mass conserved reaction–diffusion system with diffusion–driven instability. These conceptual models retained similar behaviors of cell polarity in the Rho GTPase model. Using these models, we numerically and analytically found that multiple polarized peaks are unstable, resulting in a single stable peak (uniqueness of axis), and that sensitivity toward changes of a signal gradient is specifically restricted at the polarized peak (localized sensitivity). Although molecular networks may differ from one cell type to another, the behaviors of cell polarity in migrating cells seem similar, suggesting that there should be a fundamental principle. Thus, we propose that a mass conserved reaction–diffusion system with diffusion-driven instability is one of such principles of cell polarity.

Citation: Otsuji M, Ishihara S, Co C, Kaibuchi K, Mochizuki A, et al. (2007) A mass conserved reaction–diffusion system captures properties of cell polarity. *PLoS Comput Biol* 3(6): e108. doi:10.1371/journal.pcbi.0030108

Introduction

Eukaryotic cells such as neutrophils and *Dictyostelium* cells respond to temporal and spatial gradients of extracellular signals with directional movements [1–6]. This process, known as *chemotaxis*, is a fundamental cellular process [5,7–9]. In a migrating cell, specific molecular events take place at the front and back edges [1,2,5,10]. The spatially distinctive molecular accumulation inside cells is known as *cell polarity*. The front–back polarity usually has one axis, and this uniqueness is an important property because a migrating cell with two fronts could not move effectively [11]. Another behavior of the front–back polarity is higher sensitivity of the front to a gradient of extracellular signals [10,12]. This would also be important because the direction of movement should be controlled at the front edge.

Many molecules that are involved in chemotaxis in mammalian cells have been identified [4,5]. Some molecules, including phosphoinositide 3-kinase (PI3K), phosphatidylinositol 3,4,5-triphosphate (PIP₃), Cdc42, Rac, and F-actin, are specifically localized at the front, whereas others, including phosphatase and tensin homologue deleted on Chromosome 10 (PTEN) and RhoA, are at the back of migrating cells [1,4,10,13–15]. The Rho family of small GTP(guanosine 5'-tri phosphate)ases in particular play a central role in chemotaxis and in establishing cell polarity [15–17]. However, the mechanism of generating spatial accumulation of the Rho GTPases in cell polarity has yet to be clarified.

Many mathematical models that account for gradient

sensing and signal amplification in cell polarity have been proposed [12]. The local excitation and global inhibition model has been proposed to explain spatial gradient sensing [6,18]. Some models involve positive feedback loops for amplified accumulation of signaling molecules [19–23]. A reaction–diffusion model that includes local self-enhancement and long-range antagonistic effects has been proposed for directional sensitivity [24]. Most of the reported models of cell polarity, which involve the detailed parameters such as concentrations or rate constants, have been constructed with many parameters and equations. Although these detailed models are at least partially successful in reproducing experimental observations in cell polarity, the theoretical essence underlying cell polarity has not been explicitly

Editor: Adam P. Arkin, Lawrence Berkeley National Laboratory, United States of America

Received: December 8, 2006; **Accepted:** April 29, 2007; **Published:** June 8, 2007

A previous version of this article appeared as an Early Online Release on April 30, 2007 (doi:10.1371/journal.pcbi.0030108.eor).

Copyright: © 2007 Otsuji et al. This is an open-access article distributed under the terms of the Creative Commons Attribution License, which permits unrestricted use, distribution, and reproduction in any medium, provided the original author and source are credited.

Abbreviations: GAP, GTPase-activating proteins; GDP, guanosine 5'-bis phosphate; GEF, guanine nucleotide exchange factor; GTP, guanosine 5'-tri phosphate; PI3K, phosphoinositide 3-kinase; PIP₃, phosphatidylinositol 3,4,5-triphosphate; PTEN, phosphatase and tensin homologue deleted on Chromosome 10; *u* and *v*, components of the model; *u* and *v*, concentrations of components *u* and *v*

* To whom correspondence should be addressed. E-mail: mohtsuji-ky@umin.ac.jp

Author Summary

Eukaryotic cells such as neutrophils and *Dictyostelium* cells respond to temporal and spatial gradients of extracellular signals with directional movements. In a migrating cell, specific molecular events take place at the front and back edges. The spatially distinctive molecular accumulation inside cells is known as *cell polarity*. Despite numerous experimental and theoretical studies, its mechanism of emergence has yet to be clarified. We first developed a mathematical model of the Rho small GTP(guanosine 5'-tri phosphate)ases that cooperatively regulate cell polarity, and showed that the model generates specific spatial accumulation of the molecules. Based on our Rho GTPases model and other models, we further established a conceptual model, a mass conserved reaction–diffusion system, and showed that diffusion-driven instability and a mass conservation of molecules that have active and inactive states are sufficient for polarity formation. We numerically and analytically found that molecular accumulations at multiple sites are unstable, resulting in a single stable front–back axis, and that sensitivity toward changes of a signal gradient is specifically restricted at the front of a polarized cell. We propose that a mass conserved reaction–diffusion system is one of the fundamental principles of cell polarity.

demonstrated; thus, a simple conceptual model that can be used for analytical study is needed to extract common principles in cell polarity. Although the reported models consist of distinct molecular species or networks, it should be especially emphasized that many of them are able to exhibit similar behaviors of cell polarity regardless of their different frameworks. This fact indicates that a common principle should underlie the models, and a conceptual model is suitable for extracting common principles in cell polarity.

Because the Rho small GTPases are key regulators for cell polarity [16,17], we first developed a reaction–diffusion model of the Rho GTPases on the basis of an earlier model [25] to examine the spatial properties of the Rho GTPases. We found that the interaction of the Rho GTPases per se can generate specific spatial accumulation of the Rho GTPases, and that our model shows important behaviors of cell polarity. We also found that our model exhibits behaviors similar to the model by Narang and Subramanian [22,23], which is based on the molecular networks that are different from ours. This suggests that common principles should underlie both models. We found that a mass conservation of components and diffusion-driven instability are commonly conserved in the Narang and Subramanian models and in our model. Based on these common properties, we established conceptual models of a mass conserved reaction–diffusion system, and found that such properties can account for the critical behaviors of cell polarity. These results strongly suggest that a mass conservation of components with diffusion-driven instability is one of the fundamental principles of cell polarity.

Results

The Rho GTPases Model

We developed a reaction–diffusion model of the Rho GTPases (Rac, Cdc42, RhoA) on the basis of the earlier model of the Rho GTPase [25], which explains the temporal behaviors, to examine whether the interaction of the Rho GTPases can generate the spatial behaviors in the cell polarity of migrating cells. The Rho GTPases exhibit guanine

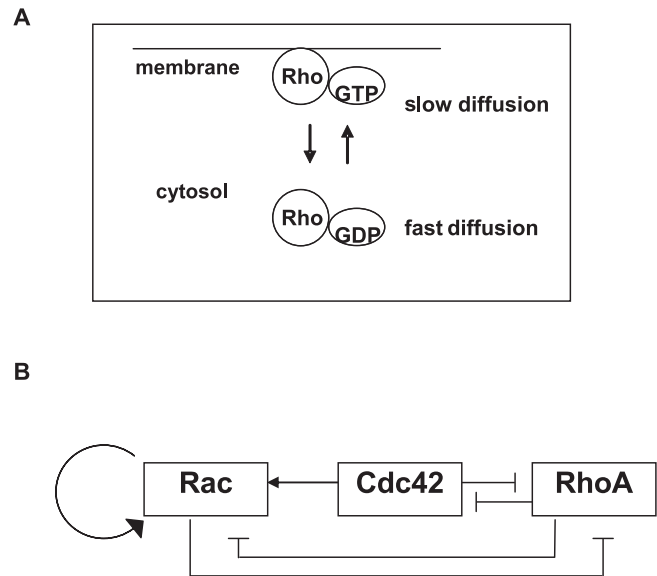


Figure 1. A Reaction–Diffusion Model of the Rho GTPases

(A) The Rho family of GTPases, which are localized in the membrane (GTP-bound active forms) or cytosol (GDP-bound inactive forms), has conserved mass and shows slower diffusion in the membrane than in the cytosol.

(B) Diagram of the model with the Rho GTPases. Arrows and bars indicate the stimulatory and inhibitory interactions, respectively.

doi:10.1371/journal.pcbi.0030108.g001

nucleotide–binding activity and function as molecular switches, cycling between an inactive GDP(guanosine 5'-bis phosphate)-bound form and an active GTP-bound form. The Rho GTPases in active forms are located in the plasma membrane, and those in inactive forms are in the cytosol (Figure 1A) [26]. It is likely that molecules in the cytosol have larger diffusivity than those in the plasma membrane. According to some studies, Cdc42 activates Rac [27–29], and RhoA has mutual inhibitory interactions with Cdc42 and Rac [29–33]. In addition, Rac plays a dominant role in a positive feedback loop, which involves PI3K, PIP₃, and F-actin [13,34–36]. Based on these experimental findings, we developed a diagram of the Rho GTPases interaction (Figure 1B). We assume that molecules of Rac, Cdc42, and RhoA are activated by guanine nucleotide exchange factors (GEFs; ka_i) and are inactivated by GTPase-activating proteins (GAPs; ki_i), and that interactions between molecules (k_{ij}) are additive to GEFs or GAPs. Some molecule–molecule interactions are stimulation dependent. Activations of molecules by the stimulation (ks_i) are also assumed to be additive to GEFs. As in many previous models [18–23], we describe the spatial kinetics of molecules by simple diffusion equations. A recent study in which the diffusion coefficients of the Rho GTPases in the plasma membrane are determined [37] may support this assumption. The model of the interaction of the Rho GTPases is as follows (see also Materials and Methods):

$$\frac{\partial Rac_m}{\partial t} = Dm_1 \frac{\partial^2 Rac_m}{\partial x^2} - (k_{13}Rho_m + ki_1)Rac_m + (k_{11}Rac_mS + k_{12}Cdc_m + ks_1S + ka_1)Rac_c,$$

$$\frac{\partial Rac_c}{\partial t} = Dc_1 \frac{\partial^2 Rac_c}{\partial x^2} + (k_{13}Rho_m + ki_1)Rac_m - (k_{11}Rac_mS + k_{12}Cdc_m + ks_1S + ka_1)Rac_c,$$

$$\begin{aligned}\frac{\partial Cdc_m}{\partial t} &= Dm_2 \frac{\partial^2 Cdc_m}{\partial x^2} \\ &\quad - (k_{23}Rho_m + ki_2)Cdc_m + (ks_2S + ka_2)Cdc_c, \\ \frac{\partial Cdc_c}{\partial t} &= Dc_2 \frac{\partial^2 Cdc_c}{\partial x^2} \\ &\quad + (k_{23}Rho_m + ki_2)Cdc_m - (ks_2S + ka_2)Cdc_c, \\ \frac{\partial Rho_m}{\partial t} &= Dm_3 \frac{\partial^2 Rho_m}{\partial x^2} \\ &\quad - (k_{31}Rac_m + k_{32}Cdc_m + ki_3)Rho_m + (ks_3S + ka_3)Rho_c, \\ \frac{\partial Rho_c}{\partial t} &= Dc_3 \frac{\partial^2 Rho_c}{\partial x^2} \\ &\quad + (k_{31}Rac_m + k_{32}Cdc_m + ki_3)Rho_m - (ks_3S + ka_3)Rho_c,\end{aligned}$$

where Rac , Cdc , and Rho with suffixes m and c denote the concentrations of Rac, Cdc42, and RhoA in the active state (membrane) and inactive state (cytosol), respectively. The numerical suffixes represent the following: 1, Rac; 2, Cdc42; and 3, RhoA. Dm_i and Dc_i denote the diffusion coefficients of molecules in the active state and inactive state, respectively ($Dm_i < Dc_i$). The position-dependent parameter, S , denotes the intensity of stimulation. Because the parameters have not been fully obtained experimentally, we set parameters to reproduce the behaviors of cell polarity (Figure 2), and further analyzed the generality of such behaviors in detail with conceptual models (see below).

Reversible accumulation of the Rho GTPases. Cell polarity accompanies exclusive reversible accumulation of Cdc42 and Rac, or RhoA, at the fronts or backs of migrating cells, respectively [4,10,13–15]. We examined the accumulation of the Rho GTPases in response to a shallow gradient of stimulation (Figure 2A–2C). The basal level of stimulation ($S = 0.1$) did not induce exclusive accumulation of the Rho GTPases (Figure 2A); however, the larger stimulation (averaged $S = 0.4$, with a slight gradient) induced accumulation of Cdc42 and Rac toward the stimulation point with the maximal intensity ($x/L = -0.2$), and exclusion of RhoA from the point (Figure 2B). The responses of accumulation and exclusion were switch-like against the intensity of stimulation (unpublished data). The accumulation and exclusion were reversed when the intensity of stimulation reduced to the basal level ($S = 0.1$) (Figure 2C).

Multiple transient peaks and a single stable peak. We next gave two points simultaneous stimulation. Cdc42 and Rac accumulated toward the stimulation points with the maximal intensity ($x/L = -0.25$ and 0.25) at $t = 60$ (Figure 2E). However, one of the accumulation peaks eventually disappeared, and only a single peak remained (Figure 2F). This result indicates that the model shows specific behaviors in cell polarity; “uniqueness of axis” (see below). The selection of the remaining peak differed between simulation tests (unpublished data).

Sensing of the stimulation gradient by the polarized peak. We next examined the behavior of the accumulation peak (polarized peak). The polarized peak moved toward the new stimulation point of the maximal intensity, rather than

generating a new peak (Figure 2G–2I). This result indicates that the polarized peak can sense a gradient of stimulation (see below).

Conceptual Model for Cell Polarity

The behaviors in the Rho GTPases model, such as switch-like reversible accumulation, uniqueness of axis, and sensing of the stimulation gradient by the polarized peak, were similar to those observed in the models of Subramanian and Narang [22,23]. Despite the differences of the molecular species and networks among the models, the similarity in behaviors among them raises the possibility that a common principle could underlie them. Therefore, we examined whether common properties can be seen. These models belong to reaction–diffusion systems with a periodic boundary condition and exhibit switch-like response, implying that instability is important for accumulation of the components. In addition, these models involve components whose masses are conserved. The total amount of phosphoinositides between the plasma membrane and the endoplasmic reticulum is conserved in Narang and Subramanian’s model [22,23], and the total amounts of the Rho GTPase between the membrane (e.g., Rho_m) and cytosol (e.g., Rho_c) are conserved in our Rho GTPases model. Based on these common properties, we derived a new concept (i.e., mass conserved reaction–diffusion system with diffusion-driven instability) and hypothesized that this system is a fundamental principle of cell polarity. We therefore developed a simple conceptual model with two components (u and v), which belong to a mass conserved reaction–diffusion system with instability, and examined whether the model can cause the behaviors of cell polarity to emerge sufficiently.

Mass conserved reaction–diffusion system. We investigated the following class of reaction–diffusion system, which is composed of two components, u and v :

$$\frac{\partial u}{\partial t} = D_u \frac{\partial^2 u}{\partial x^2} - f(u, v), \quad (1a)$$

$$\frac{\partial v}{\partial t} = D_v \frac{\partial^2 v}{\partial x^2} + f(u, v), \quad (1b)$$

$$D_u < D_v \quad (1c)$$

where u and v denote the concentrations of u and v , respectively, at time t and at position x , and D_u and D_v denote the diffusion coefficients of u and v , respectively. The reaction term f is given by a function of u and v . Because the total quantity of u and v is conserved in this case, we refer to this system as the *mass conserved reaction–diffusion system*.

We developed several models that belong to the mass conserved reaction–diffusion system and show similar results (unpublished data), and here focused on the following model because of its simplicity for computation.

Model I

$$f(u, v) = a_1 \left\{ \frac{(u + v)}{[a_2 S(u + v) + 1]^2} - v \right\}, \quad (2)$$

where a_1 and a_2 are parameters of the model. The position-

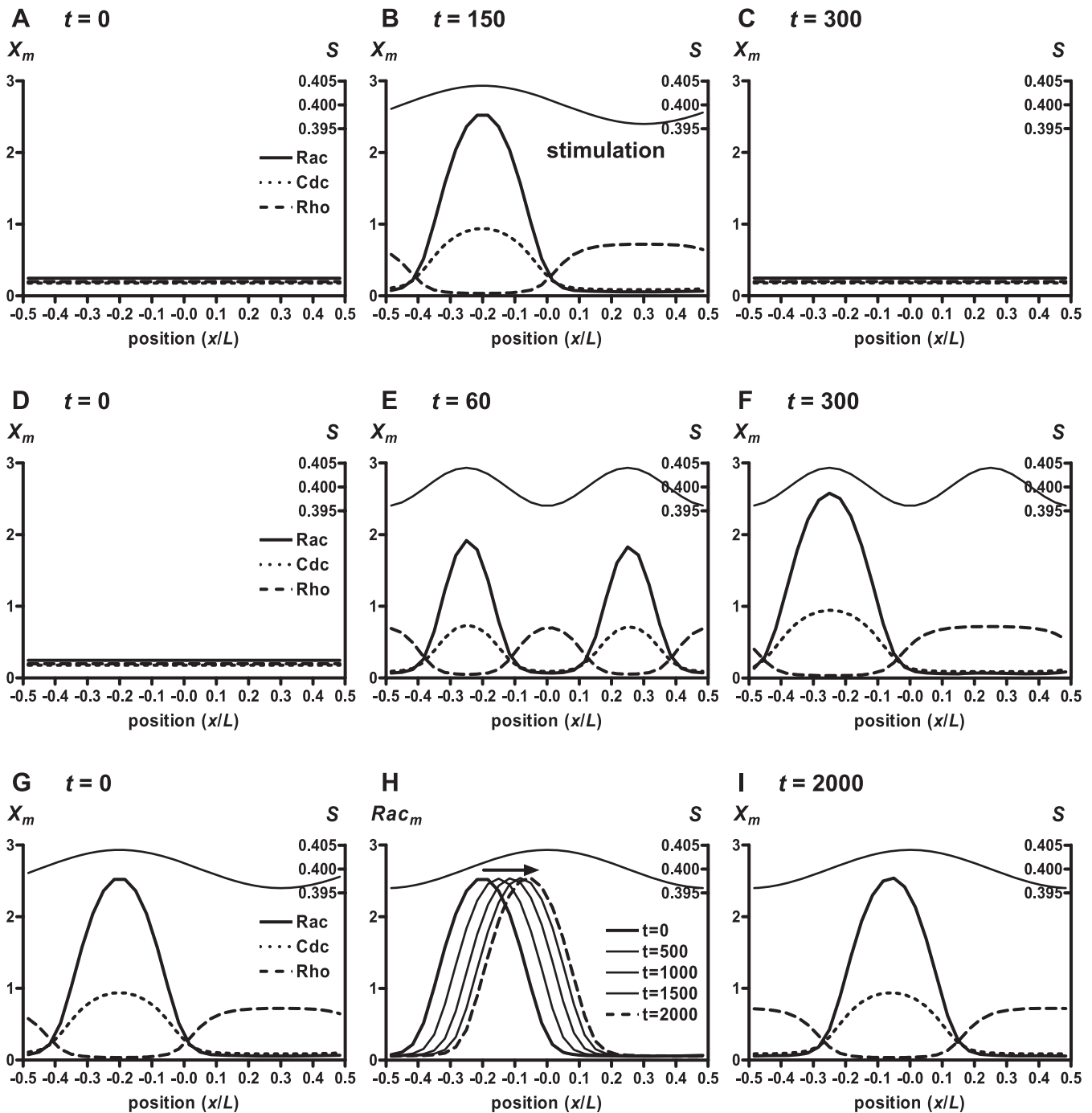


Figure 2. Behaviors of the Rho GTPases Model

Spatial profiles of Rac (solid lines), Cdc42 (dotted lines), and RhoA (dashed lines) are shown in (A–G) and (I). The thin lines in (B) and (E–I) indicate the spatial profile of the stimulation.

(A–C) Reversible accumulation of the Rho GTPases. We set $S = 0.1$ at $t = -100$, and ran the simulation until $t = 0$ to reach the stationary state (A). Then, the stimulation $S = 0.4\{1 + 0.01 \cos[2\pi(x/L + 0.25)]\}$ was given and the simulation was run until $t = 150$ to reach the stationary state (B). The stimulation point with the maximal intensity was at $x/L = -0.2$. The stimulation was reduced to the basal level ($S = 0.1$) again, and the simulation was run until $t = 300$ to reach the stationary state (C).

(D–F) Multiple transient, and a single stable, accumulation peaks. Starting with the conditions in (A), we gave random perturbation (± 0.01) to obtain the homogenous initial conditions (D). Then, at $t = 0$, the stimulation $S = 0.4\{1 + 0.01 \cos[2\pi(x/L + 0.25) \times 2]\}$ was given, and the simulation was run for the indicated time (E,F). The stimulation points with the maximal intensity were at $x/L = -0.25$ and 0.25 .

(G–I) Sensing of the stimulation gradient by the polarized peak. We set $S = 0.4\{1 + 0.01 \cos[2\pi(x/L + 0.2)]\}$ at $t = -200$, and the simulation was run to reach the stationary state where the polarized peak was seen at $x/L = -0.2$ (G). The new stimulation $S = 0.4\{1 + 0.01 \cos[2\pi(x/L)]\}$ was given, and the maximal intensity point was shifted to $x/L = 0$. The simulation was run for the indicated time (H,I). The arrow indicates the direction of movement of the polarized peak (H).

doi:10.1371/journal.pcbi.0030108.g002

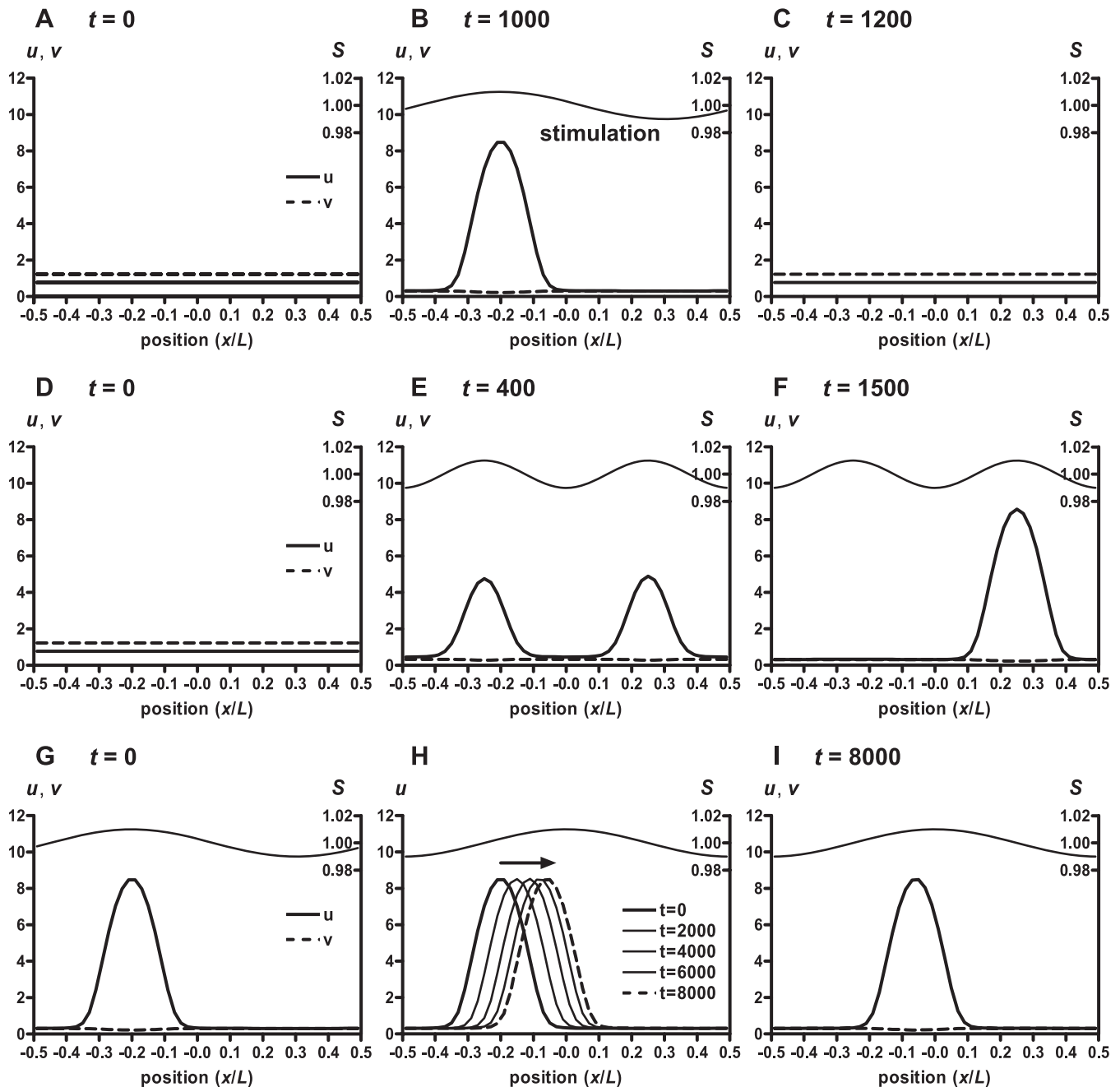


Figure 3. Behaviors of the Conceptual Model I

Spatial profiles of u (solid lines) and v (dashed lines) are shown in (A–G) and (I). The thin line in (B) and (E–I) indicates the spatial profile of the stimulation.

(A–C) Reversible accumulation of the components. We set $S = 0.2$ at $t = -100$, and ran the simulation until $t = 0$ to reach the stationary state (A). Then, the stimulation $S = 1\{1 + 0.01 \cos[2\pi(x/L + 0.2)]\}$ was given, and the simulation was run until $t = 1,000$ to reach the stationary state (B). The stimulation was reduced to the basal level ($S = 0.2$) again, and the simulation was run until $t = 1,200$ to reach the stationary state (C).

(D–F) Multiple transient and a single stable accumulation peaks. Starting with the conditions in (A), we gave random perturbation (± 0.02) to obtain the homogenous initial conditions (D). Then, at $t = 0$, the stimulation $S = 1\{1 + 0.01 \cos[2\pi(x/L + 0.25) \times 2]\}$ was given, and the simulation was run for the indicated time (E,F). The stimulation points with the maximal intensity were at $x/L = -0.25$ and 0.25 .

(G–I) Sensing of the stimulation gradient by the polarized peak. We set $S = 1\{1 + 0.01 \cos[2\pi(x/L + 0.2)]\}$ at $t = -1,000$, and the simulation was run to reach the stationary state where the polarized peak was seen at $x/L = -0.2$ (G). The new stimulation $S = 1\{1 + 0.01 \cos[2\pi(x/L)]\}$ was given, and the maximal intensity point was shifted to $x/L = 0$. The simulation was run for the indicated time (H,I). The arrow indicates the direction of movement of the polarized peak (H).

doi:10.1371/journal.pcbi.0030108.g003

dependent parameter, S , is intensity of stimulation (see Materials and Methods). The stability of the homogenous solution in this model depends on the value of S (see Materials and Methods).

We found that the conceptual model exhibits behaviors similar to the Rho GTPases model, such as switch-like reversible accumulation (Figure 3A–3C), uniqueness of axis (Figure 3D–3F), and sensing of the stimulation gradient by the

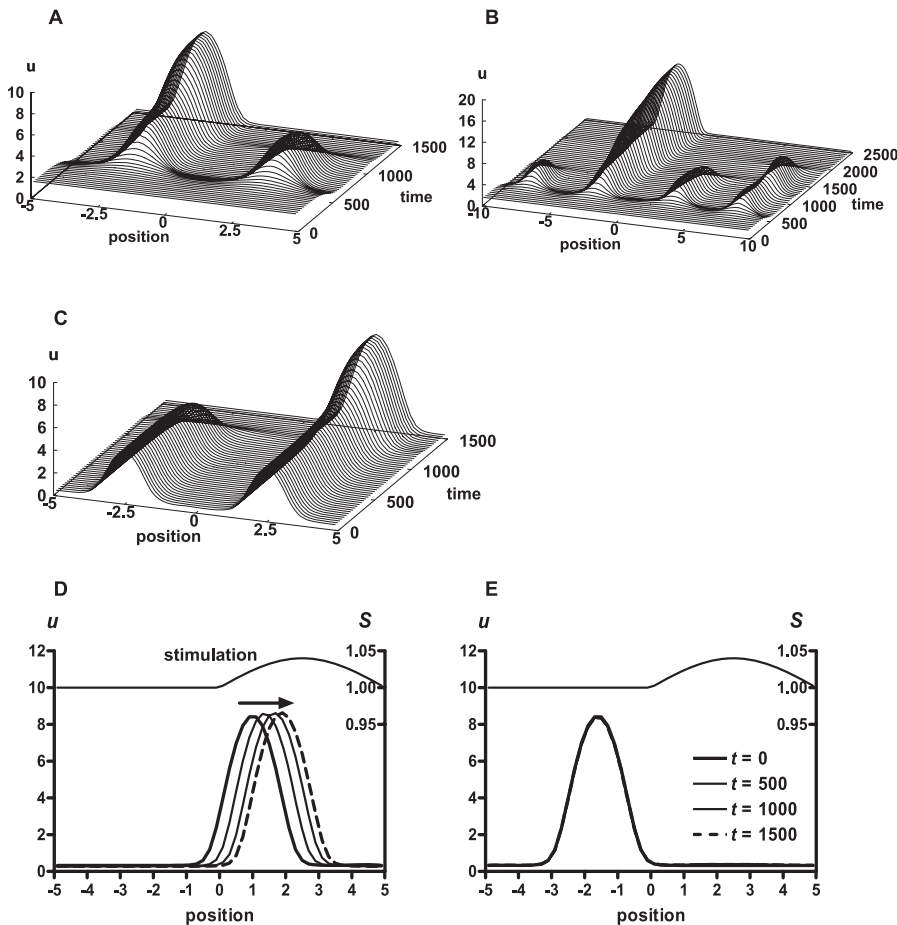


Figure 4. Numerical Evaluation of Uniqueness of Axis and Localization of Sensitivity in Model I

(A–C) Numerical evaluation of uniqueness of axis. We set $u = 1.65$, $v = 0.35$, and $S = 1$. These values of (u, v) were derived from $f(u, v) = 0$ and $u + v = 2$. The system size was taken as $L = 10$ (A) or $L = 20$ (B). We gave random perturbation (± 0.01), and the simulation was run for the indicated time (A,B). (C) Next, we obtained a stable single peak in Model I by setting $L = 5$ and taking the initial state as $u = 1.65$ and $v = 0.35$. Because we applied the periodic boundary condition to this system, we could set the center of the concentration peak at $x = 0$ by translation. By duplicating and coupling this profile ($L = 5$), we obtained a new profile ($L = 10$) with two peaks. We gave small perturbation (± 0.01) to this profile ($L = 10$), and the simulation was run for the indicated time (C).

(D,E) Numerical evaluation of localization of sensitivity. We obtained a stable single peak in Model I by setting $L = 10$ and $S = 1$, and taking the initial state as $u = 1.65$ and $v = 0.35$. We set the center of the concentration peak at $x = 1.0$ (D) or $x = -1.6$ (E) by translation. Then we gave a new stimulation $S = 1 + 0.04\cos[2\pi(x/L - 0.25)]$ ($x \geq 0$). The stimulation gradient is given only at the area of $x > 0$. The simulation was run for the indicated time (D,E).

doi:10.1371/journal.pcbi.0030108.g004

polarized peak (Figure 3G–3I). This finding indicates that the conceptual model retains the essential behaviors in the Rho GTPases model. We further used this conceptual model to examine in detail two behaviors of cell polarity: uniqueness of axis and sensitivity of the polarized peak.

Numerical evaluation of uniqueness of axis. We analyzed unstable homogenous solutions to examine the characteristic behaviors of this system by setting large homogenous S ($S = 1$) (Figure 4A and 4B). The small perturbation was given to the homogenous stationary state. This perturbation transiently induced two peaks in Model I with $L = 10$. However, one of the peaks eventually disappeared, and only a single peak remained (Figure 4A). When we doubled the system size ($L = 20$), four peaks appeared; however, as in the case with $L = 10$, only a single peak remained and others disappeared (Figure 4B). No peak arose after the first transient peaks appeared. This result suggests that the number of transient peaks depends on the system size, and that multiple transient peaks

are unstable, which results in a single peak at the final steady state.

We analyzed the relationship between the number of transient peaks and the system size by linearization analyses around the homogenous states (see Materials and Methods). For Model I (Equation 2), the wave number that grows most rapidly from homogenous state k_h^* is obtained as $k_h^* = 1.32$; the most growable wavelength is $2\pi/k_h^* = 4.78$. Therefore, the system with $L = 10$ most likely generates two peaks and the system with $L = 20$ four peaks from the homogenous states.

We further confirmed that multiple peaks are unstable. We set a two-peak profile as the initial condition, and examined its stability by giving a small perturbation. As shown in Figure 4C, the two peaks were not stable; one disappeared, and only a single peak remained. This result strongly suggests that multiple peaks are unstable, resulting in a single stable peak.

Numerical evaluation of localization of sensitivity. We examined whether the sensitivity is localized at the polarized

peak. We first induced the stable polarized peak as indicated ($t = 0$), and gave the indicated position-dependent stimulation (Figure 4D and 4E). When the polarized peak (peak at $x = 1.0$) overlapped with the gradient of the stimulation, the polarized peak moved along the gradient of S (Figure 4D); a new peak did not appear. In contrast, when the polarized peak (peak at $x = -1.6$) did not overlap with the gradient of the stimulation, the polarized peak did not move (Figure 4E); a new peak did not arise. These results indicate that the polarized peak shows sensitivity to a gradient of S , whereas the rest of the position does not show such sensitivity, and suggest that the sensitivity is restricted only at the polarized peak.

Analytical Examination of Unique Axis and Localized Sensitivity

To better understand the results of the numerical simulations, we investigated the following model (see Equations 1a–1c), by analytical approximations:

Model II

$$f(u, v) = -a_1(u + v)[(\alpha u + v)(u + v) - a_2], \quad (3)$$

where $D_u = \alpha D_v$. Here, a_1 , a_2 , and α are parameters of the models. This model belongs to the mass conserved reaction–diffusion system, and is more advantageous for analytical examination. The homogenous solution was unstable regardless of the values of parameters in this model (see Materials and Methods), so this model did not show reversible accumulation. However, the model still retained the important properties such as uniqueness of axis and localization of sensitivity, so we can use this model to analytically examine whether these behaviors can emerge from a mass conserved reaction–diffusion system with instability.

In the following sections, we show that: (1) the model has one-peak stationary states, regardless of the system size (if not too small); (2) multiple-peak stationary states are unstable; and (3) the polarized peak moves depending on the gradient of the parameter value and the sensitivity is localized. Finally, (4), we verified our analyses by comparing analytical results with the values obtained by numerical simulations.

Analysis (1): Existence of a one-peak stationary solution. We define the following variables and function:

$$N = u + v \quad (4a)$$

$$P = D_u u + D_v v \quad (4b)$$

$$f^*(N, P) = f\left(\frac{D_v N - P}{D_v - D_u}, \frac{P - D_u N}{D_v - D_u}\right). \quad (4c)$$

Equations 1a and 1b are rewritten as the following set of partial differential equations for N and P :

$$\frac{\partial N}{\partial t} = \frac{\partial^2 P}{\partial x^2}, \quad (5a)$$

$$\frac{\partial P}{\partial t} = (D_u + D_v) \frac{\partial N}{\partial t} - D_u D_v \frac{\partial^2 N}{\partial x^2} + (D_v - D_u) f^*(N, P). \quad (5b)$$

Under the periodic boundary conditions, the stationary solutions of Equations 5a and 5b, $N_e(x)$ and $P_e(x)$, satisfy the following equations:

$$P_e(x) = P_e \quad (\text{uniform}) \quad (6a)$$

$$\frac{d^2}{dx^2} N_e(x) = \frac{D_v - D_u}{D_u D_v} f^*(N_e(x), P_e). \quad (6b)$$

Consider the case of Model II given by Equation 3. For any $P_e (> 0)$, Equation 6b with the substitution of Equation 3 has a family of periodic solutions with periods between $\lambda_{min} < \lambda < \infty$ (see Materials and Methods). Here λ_{min} is given by $\lambda_{min} = 2\pi\{[D_u D_v / (D_v - D_u)](1/a_1 a_2)\}^{1/2}$. Thus, for an arbitrary large system with $L > \lambda_{min}$, one can choose a one-peak solution that satisfies the boundary conditions at $x = \pm L/2$ by taking $\lambda = L$. Note that P_e is related to λ and the average mass of $N_e(x)$, $\bar{N} = 1/L \int_{-L/2}^{L/2} N_e(x) dx$. For a sufficiently long period ($\lambda \rightarrow \infty$), this is expressed as

$$P_e \rightarrow \frac{6D_v a_2}{\lambda \bar{N}} \sqrt{\frac{D_u D_v}{D_v - D_u} \frac{1}{a_1 a_2}}. \quad (7)$$

Thus, for a sufficiently large system, $N_e(x)$ and $P_e(x)$ are approximated as:

$$N_e(x) = N_0 \text{sech}^2[b(x - x_p)], \quad (8a)$$

$$P_e(x) = P_e, \quad (8b)$$

where x_p denotes the center of the peak and b , N_0 , and P_e are constants given by:

$$b = \frac{1}{2} \sqrt{\frac{D_v - D_u}{D_u D_v} a_1 a_2}, \quad (9a)$$

$$N_0 = \frac{L \bar{N} b}{2}, \quad (9b)$$

$$P_e = \frac{3D_v a_2}{L \bar{N} b}. \quad (9c)$$

Here we obtain the one-peak solution for Model II (Equation 3) by setting an arbitrary L and \bar{N} .

Analysis (2): Stability of periodic solutions. We examined the stability of periodic solutions by linearization analysis for a single-peak solution (Analysis (2.1)) and multiple-peak solutions (Analysis (2.2)), whose periods are equal to the system size and the $1/n$ of the system size, respectively.

Analysis (2.1): Stability of a one-peak solution. First, we consider the stability of a one-peak solution given by Equations 8a and 8b. Without loss of generality, we set $x_p = 0$ here. We set $N(x, t) = N_e(x) + \Delta N(x, t)$ and $P(x, t) = P_e + \Delta P(x, t)$, and the stability is estimated by the linearized equations of Equations 5a and 5b around Equations 8a and 8b, given as follows:

$$\frac{\partial \Delta N}{\partial t} = \frac{\partial^2 \Delta P}{\partial x^2}, \quad (10a)$$

$$\begin{aligned} \frac{\partial \Delta P}{\partial t} = & (D_u + D_v) \frac{\partial \Delta N}{\partial t} - D_u D_v \frac{\partial^2 \Delta N}{\partial x^2} \\ & + (D_v - D_u)(h_N \Delta N + h_P \Delta P), \end{aligned} \quad (10b)$$

where $h_N(x)$ and $h_P(x)$ are partial derivatives of $f^*(N, P)$ by N and P , respectively, at the solution Equations 8a and 8b, that is, $h_N(x) = \partial f^*(N_e(x), P_e) / \partial N$ and $h_P(x) = \partial f^*(N_e(x), P_e) / \partial P$. Let us represent $(\Delta N, \Delta P)$ as $(e^{\mu t} n_\mu(x), e^{\mu t} p_\mu(x))$ and consider the case of Model II. Equations 10a and 10b lead to the following:

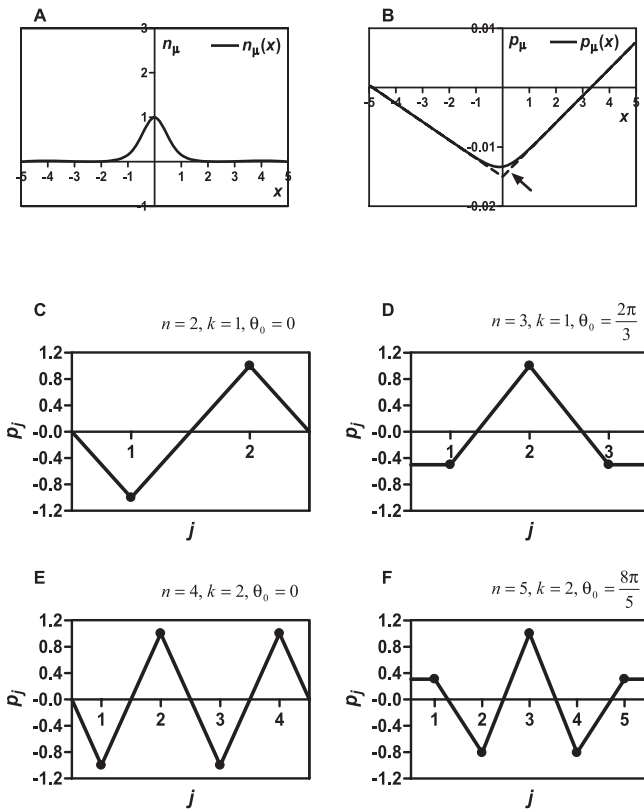


Figure 5. Stability Analysis of Multiple-Peak Solution

We seek growable perturbations (n_μ, p_μ) for the periodic solutions as discussed in the text. First, we show the perturbations for the one-peak solution, which are derived from Equations 11a and 11b, without consideration of boundary conditions: (A) $n_\mu(x)$; and (B) $p_\mu(x)$. (A,B) We used the following values: $a_1=0.5, a_2=2.2, D_u=0.1, D_v=1, \bar{N}=2$. Because we cannot determine the values of μ and C_1 without boundary conditions, we arbitrarily set $\mu=0.06$ and $C_1=0.3$ here. The dashed line with an arrow in (B) indicates the approximation to a piecewise linear function. Next, we show the perturbations for multiple-peak solutions. We can describe a perturbation by a set of p_j where p_j is the value of p_μ at the center of the j th peak. As shown in the text, we obtain p_j as $p_j^{(k)} = \cos[(2k\pi/n)j + \theta_0]$, where k is an integer ($1 \leq k \leq n/2$), corresponding to a mode, and θ_0 is an arbitrary constant. (C–F) Show the most growable perturbations for two-, three-, four-, and five-peak solutions, respectively. For each n , the mode, k , that gives the largest value to μ , is determined by $\mu^{(k)} = [(12n^3D_u a_2)/(L^3 \bar{N}^2 b)] \sin^2(k\pi/n)$. doi:10.1371/journal.pcbi.0030108.g005

$$\frac{d^2 p_\mu}{dx^2} = \mu n_\mu, \tag{11a}$$

$$\frac{d^2 n_\mu}{dx^2} = \left\{ \frac{D_u + D_v}{D_u D_v} \mu + 4b^2 [1 - 3\text{sech}^2(bx)] \right\} n_\mu - \left[\frac{\mu}{D_u D_v} + \frac{6b^2 N_0}{P_e} \text{sech}^4(bx) \right] p_\mu. \tag{11b}$$

We illustrate n_μ and p_μ in Figure 5A and 5B, respectively, for the case with $\mu > 0$ (see Materials and Methods). In the region where $|x|$ is larger than $1/b$, p_μ can be approximated as follows:

$$p_\mu \approx \begin{cases} -\frac{P_e}{N_0} + \mu \frac{-b + C_1}{b^2} x & (x < 0) \\ \frac{P_e}{N_0} + \mu \frac{b + C_1}{b^2} x & (x > 0), \end{cases} \tag{12}$$

where C_1 is a constant originated from the integral constant. This approximation is verified numerically, as shown by the dashed line with an arrow in Figure 5B. Considering periodic boundary conditions, $p_\mu(-L/2)$ and $p_\mu(L/2)$ should connect smoothly; thus, Equation 12 never satisfies Equations 11a and 11b except for $\mu = 0$.

Analysis (2.2): Instability of multiple-peak solutions. Here we consider the case of multiple-peak solutions. As long as L/n is larger than $1/b$, an identical n -peak periodic solution is approximated by:

$$N_e^j(x) = \frac{1}{n} N_0 \text{sech}^2(x - x_p^j), \tag{13a}$$

$$P_e^j(x) = n P_e, \tag{13b}$$

on each j th domain defined as $x_p^j - L/2n \leq x \leq x_p^j + L/2n$, where x_p^j is the position of each peak j ($j = 1, \dots, n$) given by $x_p^j = -L/2 + (j - 1/2)L/n$. We set $\Delta P = P(x, t) - P_e^j(x) = e^{\mu t} p_\mu^j$. As in the case of the one-peak solution, we can obtain

$$p_\mu \approx \begin{cases} n_0^j \left[-\frac{n^2 P_e}{N_0} + \mu \frac{-b + C_1^j}{b^2} (x - x_p^j) \right] & (x < x_p^j) \\ n_0^j \left[-\frac{n^2 P_e}{N_0} + \mu \frac{b + C_1^j}{b^2} (x - x_p^j) \right] & (x > x_p^j). \end{cases} \tag{14}$$

for each j th domain. For multiple-peak solutions, n_0^j and C_1^j are determined by the boundary conditions such that p_μ^j connect smoothly between adjacent domains. This piecewise linear function takes the value $p_j = -n_0^j n^2 P_e / N_0$ at $x = x_p^j$, and at the point the slope changes by $-\mu(2N_0/n^2 P_e b) p_j$. A smooth connection between them means the slope is given as $(p_{j+1} - p_j)/(L/n)$ for $x_p^j < x < x_p^{j+1}$. Thus, p_j satisfies the following relationship:

$$\frac{p_{j+1} - p_j}{L/n} - \frac{p_j - p_{j-1}}{L/n} = -\mu \frac{2N_0}{n^2 P_e b} p_j. \tag{15}$$

Considering periodic boundary conditions, we obtain the following solutions:

$$p_j^{(k)} = \cos\left(\frac{2k\pi}{n} j + \theta_0\right), \tag{16a}$$

$$\mu^{(k)} = \frac{2n^3 P_e b}{N_0 L} \sin^2\left(\frac{k\pi}{n}\right) = \frac{12n^3 D_u a_2}{L^3 \bar{N}^2 b} \sin^2\left(\frac{k\pi}{n}\right), \tag{16b}$$

where k is an integer ($1 \leq k \leq n/2$), corresponding to a mode, and θ_0 is an arbitrary constant. All modes have positive μ , and therefore can grow. Figure 5C–5F shows the most growable mode for the n -peak solution ($n = 2, 3, 4, 5$), that gives the largest value to μ .

Based on this analysis, the one-peak solution is stable, whereas the multiple-peak solutions are unstable, regardless of the parameter values.

Analysis (3): Response of the polarized peak to a position-dependent parameter. Here we study the case in which the system has a position-dependent parameter by substituting $a_2^*(x) = a_2 + \epsilon a_\epsilon(x)$ for a_2 in Equation 3, where $|\epsilon a_\epsilon(x)|$ is sufficiently smaller than a_2 . It is useful to represent the explicit dependence of f^* on the parameter, as $f^*(N, P, a_2^*)$. In this case, an existing peak moves, as is the case with Model I (Figure 3G–3I). To derive the velocity of the peak (v_p), we define the following variable and functions:

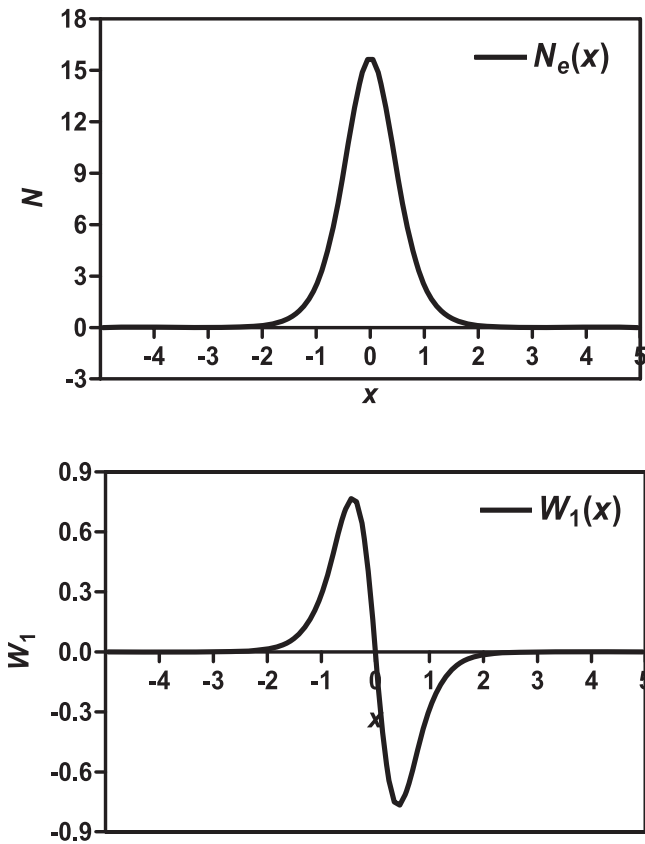


Figure 6. Sensing Window of the Polarized Peak That Detects the Position Dependence of a Parameter
 The velocity of the polarized peak responding to a parameter gradient is determined by $\int_{-L/2}^{L/2} W_1(x)\varepsilon G_a(x) dx$, where $\varepsilon G_a(x)$ represents the position dependence of the parameter. Here we can regard $W_1(x)$ as a sensing window. The upper panel shows the profile of the polarized peak, $N_e^*(x)$; the lower panel indicates $W_1(x)$.
 doi:10.1371/journal.pcbi.0030108.g006

$$z = x - v_p t, \tag{17a}$$

$$N^*(z, t) = N(z + v_p t, t), \tag{17b}$$

$$P^*(z, t) = P(z + v_p t, t). \tag{17c}$$

Equations 5a and 5b are rewritten as the following set of partial differential equations for N^* and P^* :

$$\frac{\partial N^*}{\partial t} - v_p \frac{\partial N^*}{\partial z} = \frac{\partial^2 P^*}{\partial z^2}, \tag{18a}$$

$$\begin{aligned} \frac{\partial P^*}{\partial t} - v_p \frac{\partial P^*}{\partial z} &= (D_v + D_u) \left(\frac{\partial N^*}{\partial t} - v_p \frac{\partial N^*}{\partial z} \right) \\ &- D_u D_v \frac{\partial^2 N^*}{\partial z^2} + (D_v - D_u) f^*(N^*, P^*, a_2^*). \end{aligned} \tag{18b}$$

Under the periodic boundary conditions, the stationary solutions of Equations 18a and 18b, $N_e^*(z)$ and $P_e^*(z)$, satisfy the following equations:

$$-v_p \frac{\partial N_e^*}{\partial z} = \frac{\partial^2 P_e^*}{\partial z^2}, \tag{19a}$$

$$\begin{aligned} -v_p \frac{\partial P_e^*}{\partial z} &= (D_v + D_u) \left(-v_p \frac{\partial N_e^*}{\partial z} \right) \\ &- D_u D_v \frac{\partial^2 N_e^*}{\partial z^2} + (D_v - D_u) f^*(N_e^*, P_e^*, a_2^*). \end{aligned} \tag{19b}$$

Considering that $\varepsilon = 0$ and $v_p = 0$ lead to $N_e^*(z) = N_0 \operatorname{sech}^2(bz)$ and $P_e^*(z) = P_e$, we can set $N_e^*(z) = N_0 \operatorname{sech}^2(bz) + n_\varepsilon(z)$ and $P_e^*(z) = P_e + p_\varepsilon(z)$ for small value of ε . The linearized approximations of Equations 19a and 19b around $(N_e^*, P_e^*, a_2^*) = (N_0 \operatorname{sech}^2(bz), P_e, a_2)$ give us the velocity of the peak at $t = 0$ (see Materials and Methods):

$$v_p = \frac{- \left[\int_{-L/2}^{L/2} W_1(x) \varepsilon G_a(x) dx \right]}{b N_0 Z}, \tag{20}$$

where $W_1(x) = -2 \tanh(bx) \operatorname{sech}^2(bx)$, and Z is a constant. $G_a(x)$ is defined by $G_a(x) = (4b^2 N_0 / a_2) \operatorname{sech}^2(bx) a_\varepsilon(x)$, which reflects the position dependence of $a_2^*(x)$.

Equation 20 indicates that the velocity of the peak is determined by the integral of $W_1(x) \varepsilon G_a(x)$ with respect to x . Taking into consideration that $\varepsilon G_a(x)$ represents the position dependence of $a_2^*(x)$ and that the position dependence at the site where the value of $W_1(x)$ is trivial has little influence on the velocity, we can regard $W_1(x)$, which is a kind of weight function, as a “sensing window.” As shown in Figure 6, this window has significant value only at the site of the concentration peak. Indeed, as for the mass conserved reaction–diffusion system, $W_1(x)$ is proportional to dN_e^*/dx , and thus the sensing window is locally open at the preexisting peak, especially at the peripheries of the peak. Note that the integral of $W_1(x) \varepsilon G_a(x)$ is zero when $a_\varepsilon(x)$ is an even function; therefore, the sensing window can detect a gradient (or slope) of $a_2^*(x)$.

Based on this analysis, the polarized peak can detect the position dependence of a parameter and move depending on the gradient at the site of the peak. This property can be called “localized sensitivity.”

Analysis (4): Verification of analysis by computations. Finally, in Analyses (4.1)–(4.3), we verified our Analyses (1)–(3), respectively, by comparing analytical results with the values obtained by numerical simulations.

Analysis (4.1): Approximation of the one-peak solution. First, we verify the results of Analysis (1): Existence of a one-peak stationary solution. We obtain analytical approximations of the one-peak solution as Equations 8a and 8b, and we compare this approximation with the final profile of the numerical simulation of Model II. The left panel of Figure 7A is the final profile of numerical simulation (see Materials and Methods). The solid line indicates the profile of N , and the dashed line indicates P . The right panel of Figure 7A shows the approximations given by Equations 8a and 8b, taking the center of the peak as $x_p = -2.15$. The results of the computations show good agreement with our analytical results. The approximations were also sufficient when we set $L = 20, 40,$ and 80 (unpublished data).

Analysis (4.2): Instability of a two-peak solution. Next, we verify the results of Analysis (2.2): *Instability of multiple-peak solutions.* According to our analysis, a two-peak solution is unstable, and perturbations will grow exponentially with a growth rate μ_{ant} given by Equation 16b with $n = 2$ and $k = 1$, that is, $\mu_{ant} =$

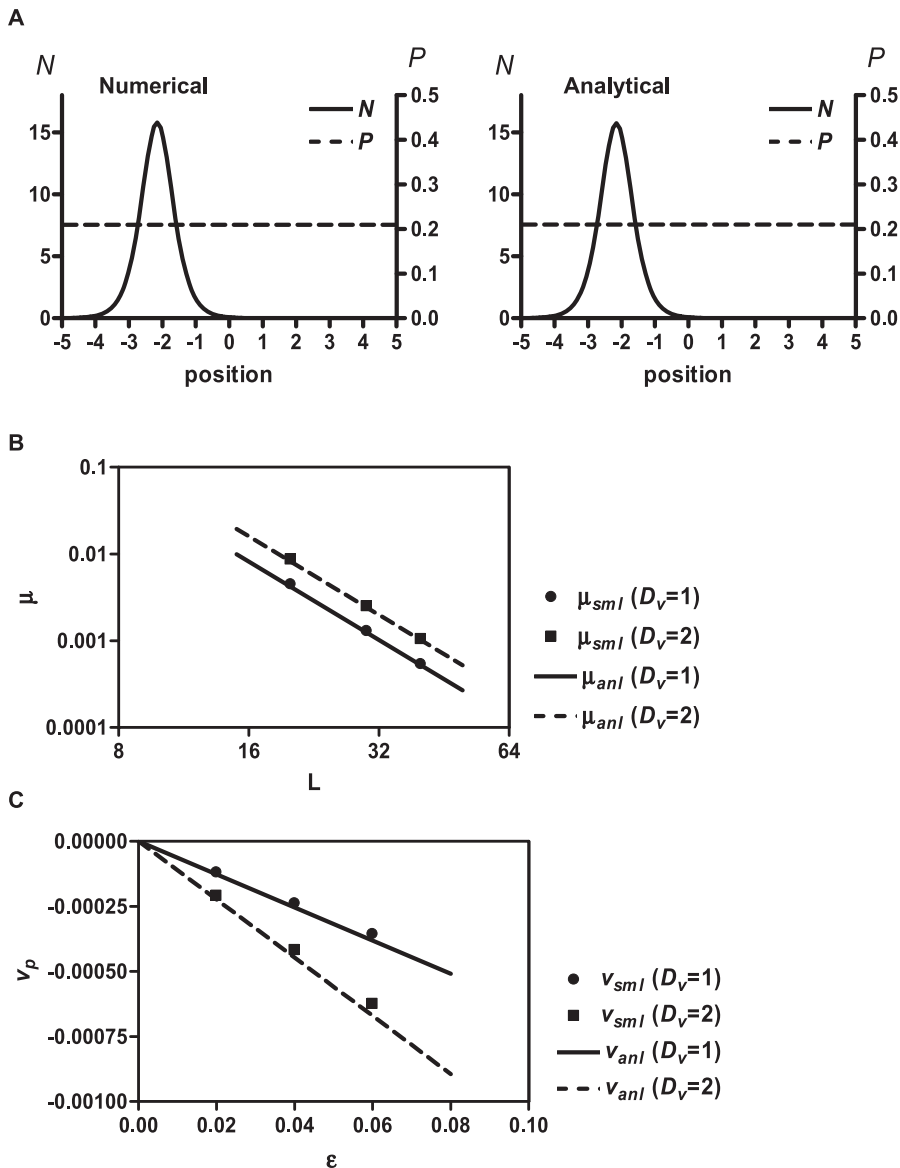


Figure 7. Verification of Analysis by Computations

(A) Approximation of one-peak solution. The left panel indicates the result of numerical simulation (Model II); the right panel indicates the analytical approximation.

(B) Instability of the two-peak solution. A two-peak state is unstable in Model II and some perturbation grows. We compare the growth rates estimated by analysis with those obtained by simulations. For simulations, we varied D_v ($= 1$ or 2) and L ($= 20, 30,$ or 40); thus, six trials were performed. The axes indicate μ and L in double logarithmic scales.

(C) Movement of polarized peak is dependent on the parameter gradient. An existent peak moves when a gradient is given to the parameter. We compare the velocity estimated by analysis with those obtained by simulations. For simulations, we varied D_v ($= 1$ or 2) and ϵ ($= 0.02, 0.04,$ or 0.06); thus, six trials were performed.

doi:10.1371/journal.pcbi.0030108.g007

$(96D_v a_2)/(L^3 \bar{N}^2 b)$. We numerically examined the growth rate of the perturbation given to two-peak solutions with $D_v = 1, 2,$ and $L = 20, 30, 40$ (see Materials and Methods). We logarithmically plotted the growth rates estimated by analytical results (μ_{ani} ; Figure 7B, solid and dashed lines) and those obtained by numerical simulations (μ_{smi} ; Figure 7B, filled circles and squares) against the system size L . The results of the analyses and computations were nearly identical.

Analysis (4.3): Movement of a polarized peak in response to the parameter gradient. Finally, we verify the results of Analysis (3): Response of the polarized peak to a position-dependent parameter.

According to our analysis, the polarized peak will move

when a parameter gains position dependence. A concentration peak formed in Model II (Equation 3) with uniform a_2 will move when a_2 is replaced by $a_2^*(x) = a_2\{1 + (\epsilon/2)\sin[2\pi(x/L)]\}$ with a velocity v_{ani} obtained by Equation 20 as:

$$v_{ani} = - \frac{\int_{-L/2}^{L/2} [\tanh(bx)\text{sech}^4(bx)\sin(2\pi x/L)] dx}{\frac{16}{15} \left[\frac{D_v + D_u}{D_v - D_u} \frac{1}{a_1 a_2} + \frac{L^2 \bar{N}^2}{6D_v a_2} \left(\frac{3}{7} - \frac{1}{bL} \right) \right]} \epsilon. \quad (21)$$

We numerically examined the velocity of movement of the polarized peak in response to a parameter gradient with $D_v = 1, 2,$ and $\epsilon = 0.02, 0.04, 0.06$ (see Materials and Methods). We

plotted the velocities estimated by analytical results (v_{ani} ; Figure 7C, solid and dashed lines) and those obtained by numerical simulations (v_{smi} ; Figure 7C, filled circles and squares) against the parameter gradients ϵ . The results of the analyses and computations were nearly identical.

Discussion

Rho GTPases and Conceptual Model

In this study, we used a mathematical model to clarify the role of the interaction between the Rho GTPases in cell polarity and developed a conceptual model of cell polarity to glean a theoretical understanding of the unique behaviors of cell polarity.

The Rho GTPases regulate the remodeling of the actin cytoskeleton via actin polymerization, depolymerization, and myosin activity [15,17,26], which ultimately establishes cell polarity. Then, what regulates the spatial activity of the Rho GTPases? The model proposed by Sakumura et al. indicates that the interaction of the Rho GTPases can regulate their own temporal activities [25]. We demonstrated that the interaction of the Rho GTPases can regulate their own spatial activities. In reality, the interaction of the Rho GTPases can provide more complicated temporal and spatial regulation of their activities. Further study, including the determination of kinetic parameters of the interaction, is necessary to develop a more realistic model of the Rho GTPases.

The activator–inhibitor model for pattern formation [38] and the local excitation and global inhibition model for directional sensing in chemotaxis [6] belong to conceptual models, rather than to detailed biological models. Such conceptual models with reduction of equations and parameters make analysis simpler and clearer. We identified a mass conserved reaction–diffusion system with instability as common properties between the cell polarity models. The model belonging to this system can sufficiently reproduce the important behaviors of cell polarity, such as uniqueness of axis and localization of sensitivity, and enabled us to theoretically understand such behaviors, which are difficult to examine without the models.

Uniqueness of Axis and Localization of Sensitivity

When interleukin-8, a chemoattractant, is applied simultaneously from two directions at a 45° angle, normal neutrophils choose one direction for migration instead of responding to both sources [11]. Neutrophils with multiple leading edges are rarely observed under normal conditions [39]. When HL60 cells are transfected with a dominant-negative Rho construct or treated with Rho-kinase inhibitors, many cells exhibit the multiple pseudopods, where, in some cells, protrusions gradually withdraw, leaving a single, prominent pseudopod [10]. In addition, inhibitions of PI3Ks cause HL-60 cells to form multiple pseudopods, which are weak and transient [39]. These results suggest the instability of multiple leading edges, which may make the front of a migrating cell single and stable. Chemotactic cells must have only one front–back axis because multiple fronts would prevent fine migration. Subramanian and Narang investigated the response of their model to two almost identical stimulations [23] and showed that only one of the two peaks that arise persists, which agrees with our results. Here we show that uniqueness of axis emerges from instability of

multiple peak solutions in a mass conserved reaction–diffusion system (Figures 4C and 5).

In neutrophils [40], HL-60 cells [10], and *Dictyostelium* cells [41], the polarized cells respond to changes in direction of a gradient by performing U-turns rather than by simply reversing polarity. In addition, polarized migrating cells move forward without responding to the chemoattractant source near their rears [12]. These experimental findings indicate that the sensitivity to chemoattractants is localized at the leading edge of polarized cells. The localized sensitivity focuses the activity of the actin cytoskeleton at the leading edge, resulting in faster movement toward a chemoattractant source [12]. Few mathematical theories, however, have been proposed to explain the localization of sensitivity. Here we show that localization of sensitivity depends on the specific localization of a sensing window at the polarized peak in a mass conserved reaction–diffusion system (Figure 4D and 4E and Figure 6). It should be added that many other systems can also exhibit a localized sensing window.

Biological Interpretation of Mass Conservation

Consider a molecule that satisfies the following conditions: (1) the molecule (X) has two states (X_m and X_c); (2) the total amount of X is conserved; and (3) the diffusion coefficient of X_c is larger than that of X_m. Two states of this molecule can be treated as components of a mass conserved system. Some kinds of small GTPases, such as those of the Rho family, have two forms, active and inactive forms; the Rho GTPases in the active forms are located in the membrane, and those in the inactive forms are in the cytosol [26]. Some enzymes involved in the cell polarity of chemotactic cells, such as PI3K and PTEN, are also reported to show a relationship between their activity and membrane binding [42–46]. Molecules in the cytosol may well diffuse faster than those in the plasma membrane. Thus, these molecules can be considered as components of mass conserved systems.

Chemotactic cells, such as *Dictyostelium* cells and neutrophils, polarize within a few minutes (30 s to 3 min) after they are exposed to chemoattractants [6,10,47]. Because the time scale of cell polarity is likely to be much shorter than that of gene expression and protein synthesis, we can assume that the masses of molecules are constant during the polarization of chemotaxis.

Instability of Multiple-Peak Solutions

We numerically and analytically show that multiple-peak solutions are unstable. To facilitate an understanding of the physics of this instability, we attempt to give an intuitive physical explanation of the behavior of molecules in the case where there exist two peaks (Figure 8), just as in Figure 4C. We simplify the situation as follows. (1) There are two spaces (each space has one peak). (2) The molecules have two forms, u and v, which have small and large diffusivities, respectively. (3) No molecule is generated or degraded in the spaces. (4) The molecules move between spaces, mainly in v-form, depending on the concentration gradient of v-form molecules. (5) The u-form molecules convert v-form molecules into u-form, and this positive feedback is so strong that infusion of molecules into the space causes a decrease in v-form molecules. Here, consider that a few molecules move from one space (S1) to the other (S2). According to (5), because of the nature of the positive feedback, the number of

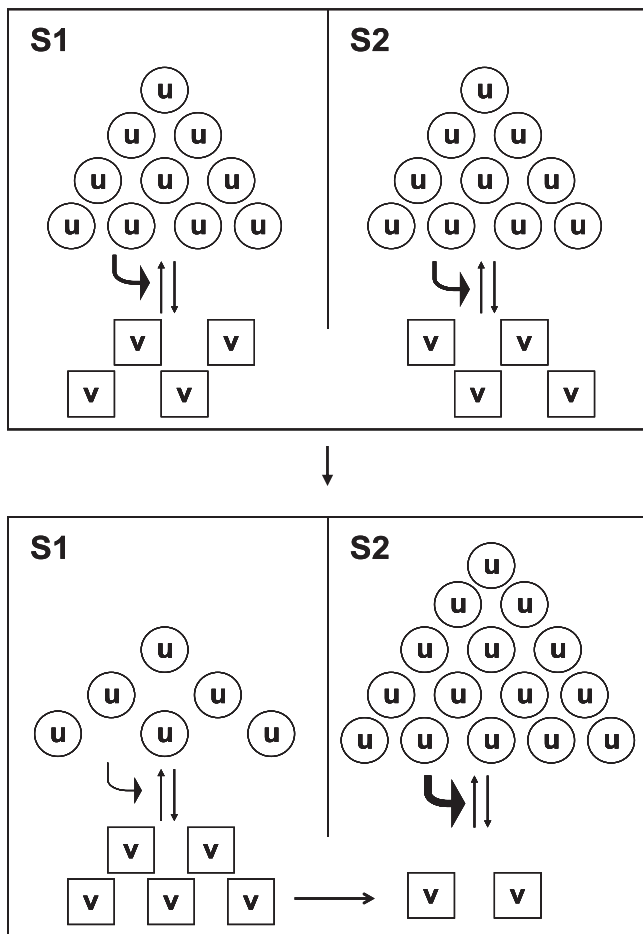


Figure 8. Schematic of Unstable Multiple-Peak Solution in a Mass Conserved Reaction–Diffusion System

We set the two-peak solution (S1 and S2, top panel), which is similar to Figure 4C. We consider the following conditions. There are two spaces (each space has one peak). The molecules have two forms, u and v , which have small and large diffusivities, respectively. No molecule is generated or degraded in the spaces. The molecules move between spaces, mainly in v -form, depending on the concentration gradient of v -form molecules. The u -form molecules convert v -form molecules into u -form, and this positive feedback is so strong under the condition where $\partial P_u / \partial N < 0$ [48] that infusion of molecules into the space causes a decrease in v -form molecules. Infusion of molecules to S2 accompanies the removal of the same number of molecules from S1 because of the mass conservation (bottom panel).

doi:10.1371/journal.pcbi.0030108.g008

v -form molecules in S2 declines as the total number of molecules in S2 increases. In turn, according to (4), the declining of the number of v -form molecules in S2 successively facilitates further transfer of v -form molecules from S1 to S2, resulting in the further increase of the total number of molecules in S2. This flux is never disrupted by the generation or degradation of molecules because of the mass conservation. Therefore, two peaks in such a system are unstable. The condition (5) seems critical for instability, and we analyzed such conditions mathematically elsewhere [48].

Specific Feature of the Mass Conserved Reaction–Diffusion System

One of the most extensively studied reaction–diffusion models is the Turing model, in which robust spatial patterns, such as stripes or spots, emerge via a diffusion-driven

instability [38,49]. An ordinary Turing pattern in 1-D space is stripes with an intrinsic scale length [50]. Mass conserved models also generate multiple peaks from the homogenous state during the early phase, which is explained by diffusion-driven instability. However, they exhibit characteristic transitions after the initial peaks arise: most peaks become smaller and eventually disappear, and only one peak persists (Figure 4A and 4B). Why is the behavior of the mass conserved system so different from that of ordinary Turing models? Consider a reaction–diffusion system with vast size ($L \rightarrow \infty$) and interval $I [x_1, x_2]$ within the system, where x_1 and x_2 are arbitrary but far apart. Can we predict what will happen to interval I ? For an ordinary Turing model, the linearization analysis around the homogenous solution gives us sufficient information [50]. The mass conserved system is more complex, however, because the behavior differs between the case where the components flow into interval I versus the case where they flow out, and we cannot predict which will occur. This difference in predictability seems to be fundamentally linked to the different behavior and the specificity of the mass conserved system. Mass conserved models have multiple stationary states that are spatially homogenous or periodic, including a one-peak state and multiple-peak states. We show that the multiple-peak stationary states are unstable, resulting in a single stable peak.

In some reaction–diffusion systems, such as the activator–inhibitor model (or substrate–depleted model), high diffusivity of inhibitor (or substrate) make multiple peaks unstable, resulting in a single stable peak [51]. An intuitive explanation for this instability is that an inhibitor, which is generated at the peak, rapidly diffuses throughout the cell. In the cell where the inhibitor can be generated and degraded, the spread of the inhibitor requires the large diffusivity to overwhelm the inhibitor degradation. On the other hand, in a mass conserved reaction–diffusion system, where no molecule is generated or degraded, a peak takes up molecules from its surroundings to grow. That is, the growing peak inhibits the system not by spread of inhibitor but by deprivation of molecules. In this case, large diffusivity is not required because there is no competitor to overcome, such as generation of molecules, and the inhibition can eventually spread throughout the cell. Indeed, Equation 16b clearly indicates that any D_v can make multiple peaks unstable ($\mu > 0$), at least in Model II.

It may be counterintuitive that any mass conserved system finally exhibits a one-peak pattern. For Model II, the final steady state was a one-peak solution regardless of the system size, even when L was infinitely large. But for Model I, the final steady state had two peaks when we set $L = 80$ (unpublished data). Some mass conserved models probably have a maximum size to have a unique peak. However, this maximum size is independent of the linearization analysis. The conditions for the uniqueness of concentration peak will be elucidated in future analyses.

Future Perspective and Conclusion

Because properties observed in simple models are expected to be conserved in more detailed models, we assume that movement of molecules follows a simple diffusion equation in our conceptual model. Active transport systems, such as actomyosin- and microtubule-based active transports, regulate cell polarity in various cellular processes [52]. Such active

transports are likely to follow the formation of intracellular asymmetry, which takes place under the resting condition where the cell polarity is yet to be generated. Under such conditions, the diffusion of the Rho small GTPases has been measured and shown to be approximated by an apparent simple diffusion, if viewed on the order of seconds or tens of seconds [37]. Because our concern in this study is the earlier asymmetry formation rather than the completion of the polarity, which includes active transport, we here assumed the simple diffusion of the Rho GTPases. However, we will readily incorporate the detailed mechanism of the transport system of the Rho–GTPases in a future model.

In this study, we focused on the stationary state, but not on the transient state, which involves adaptation in response to a transient signal [44,53–55]. Such properties, as well as high dimensionality and multiple components, should be incorporated into a future model.

Although our model is rather simple, it shows the important properties of cell polarity such as switch-like reversible response, uniqueness of axis, and localization of sensitivity. We further demonstrated that the instability of multiple-peak solutions and the specific localization of a sensing window at the polarized peak in a mass conserved reaction–diffusion system are responsible for uniqueness of axis and localization of sensitivity, respectively. One remarkable feature of a mass conserved reaction–diffusion system compared with other models is that a mass conserved reaction–diffusion system does not require strict assumptions for diffusion coefficients, such as smaller and much larger diffusivities of excitatory and inhibitory molecules, respectively, in the local excitation and global inhibition models [6,18], or an extraordinary large diffusivity of the inhibitor in the Gierer–Meinhardt model [51]. Since the Rho GTPases, PI3K, or PTEN have thus far not been demonstrated to involve such ad hoc assumptions of diffusivity, a mass conserved reaction–diffusion system is more likely to explain cell polarity where these molecules are involved, and to be adapted to a wide range of cell polarity. Taking into consideration that the Rho GTPases system satisfies conditions of a mass conserved reaction–diffusion system, it is likely that this system is one of the fundamental principles of cell polarity.

Materials and Methods

Simulation. We considered a one-dimensional circular system with circumference L . The position is represented by x ($-L/2 \leq x \leq L/2$). We applied the periodic boundary condition, which is used in some models that explain cell polarity [23,24]. We used explicit difference methods to perform simulations. The difference intervals for calculations are shown in the following text.

Simulation of the Rho GTPases model. The parameter values were set as follows: $L = 10$, $Dm_i = 0.04$, $Dc_i = 3$ ($i = 1, 2, 3$), $ks_1 = 1$, $ks_2 = 1$, $ks_3 = 1$, $ka_1 = 0.2$, $ka_2 = 0.2$, $ka_3 = 0.2$, $ki_1 = 0.4$, $ki_2 = 0.2$, $ki_3 = 0.2$, $k_{11} = 4$, $k_{12} = 3$, $k_{13} = 5$, $k_{23} = 6$, $k_{31} = 4$, and $k_{32} = 2$. The difference intervals for calculations were taken to be $\Delta t = 0.01$ and $\Delta x = 0.33$. We set $X_m(x) = 0.3$, $X_r(x) = 0.7$ ($X = Rac, Cdc, Rho$), unless specified.

Simulation of Model I. The parameter values were set as follows: $a_1 = 2.5$, $a_2 = 0.7$, $D_u = 0.01$, $D_v = 1$, and $L = 10$. The difference intervals for calculations were taken to be $\Delta t = 0.01$ and $\Delta x = 0.2$. We set $u = 1$ and $v = 1$, unless specified.

Simulation of Model II for Analysis (4). The parameter values were set as follows: $a_1 = 0.5$, $a_2 = 2.2$, $D_u = 0.1$, $D_v = 1$ or 2 , $\bar{N} = 2$. The difference intervals for calculations were taken to be $\Delta t = 0.005$ and $\Delta x = 0.2$.

Approximation of a one-peak solution. The computation was performed by setting $L = 10$ and $D_v = 1$ and taking the initial state as $u = 1$ and $v =$

1 with small perturbation (± 0.01). The final profile ($t = 200$) is shown in the left panel of Figure 7A. The solid line indicates the profile of N , and the dashed line indicates P .

Instability of a two-peak solution. We examined the instability of two-peak solutions. First, we obtained a stable one-peak pattern in Model II (Equation 3) by taking the size to be $L/2$, where $L = 20, 30, 40$, and taking the initial state as $u = 1$ and $v = 1$ with small perturbation (± 0.01). Because we applied the periodic boundary condition to this system, we could set the center of the concentration peak at $x = 0$ by translation. Next, by duplicating and coupling this profile ($L/2$), we obtained a new profile (L) with two peaks. We used this profile (L) with small perturbations (± 0.01) as the initial state of the following simulation. All trials ($D_v = 1, 2$ and $L = 20, 30, 40$) showed instabilities of two-peak profiles, and we obtained the growth rate, μ_{smb} from the change in peak height.

Movement of a polarized peak in response to the parameter gradient. We examined the response to the parameter gradient. First, we obtained a stable one-peak pattern in Model II (Equation 3) by setting $L = 10$ and taking the initial state as $u = 1$ and $v = 1$. We set the center of the concentration peak at $x = 0$ by translation. Next, we substituted $a_2^*(x) = a_2\{1 + (\varepsilon/2)\sin[2\pi(x/L)]\}$ for a_2 in Equation 3. All trials ($D_v = 1, 2$ and $\varepsilon = 0.02, 0.04, 0.06$) showed movement of the polarized peaks, and we obtained the velocities, v_{smb} from the results.

Linearization analysis around the homogenous state. In the homogenous stationary state, the Jacobian matrix for the reaction terms is given by

$$J = \begin{pmatrix} -f_u & -f_v \\ f_u & f_v \end{pmatrix}, \quad (22)$$

where f_u and f_v denotes the partial derivatives of f by u and v , respectively, at a homogenous stationary state of Equations 1a and 1b. We obtained a condition for instability of the homogenous solution: $(D_u f_v - D_v f_u)/(D_u D_v) > 0$. For example, the homogenous solution is stable with $S = 0.2$ in Model I, whereas unstable with $S = 1$, under the following conditions: $a_1 = 2.5$, $a_2 = 0.7$, $D_u = 0.01$, $D_v = 1$, $u + v = 2$. The homogenous solution in Model II is always unstable.

Through the stability analysis using J , the range of wave numbers (k_h) that have positive eigenvalues is obtained as $0 < k_h < [(D_u f_v - D_v f_u)/(D_u D_v)]^{1/2}$, and the wave number that has the largest eigenvalue and grows most rapidly from the homogenous state, k_h^* , is obtained as follows:

$$k_h^* = \left\{ \frac{1}{D_v - D_u} \left[(f_u + f_v) + \left(\sqrt{\frac{D_v}{D_u}} + \sqrt{\frac{D_u}{D_v}} \right) \sqrt{f_u f_v} \right] \right\}^{1/2}. \quad (23)$$

For Model I (Equation 2), we obtain $k_h^* = 1.32$ under the following conditions: $a_1 = 2.5$, $a_2 = 0.7$, $D_u = 0.01$, $D_v = 1$, $S = 1$, $u + v = 2$.

Periodic solution of Equation 6b. Equation 6b has the same formulation as classical Newton mechanics. We define $V(N_e)$ as

$$V(N_e; P_e) = -\frac{D_v - D_u}{D_u D_v} \int_0^{N_e} f^*(N, P_e) dN, \quad (24)$$

and Equation 6b implies

$$dx = \frac{dN_e}{\sqrt{2[E - V(N_e; P_e)]}}, \quad (25)$$

where E is a constant value, corresponding to period and total mass of $N_e(x)$. The period λ and the average mass $\bar{N} = (1/\lambda) \int_0^\lambda N_e(x) dx$ satisfy the following equations:

$$\lambda = 2 \int_{N_{min}}^{N_{max}} \frac{dN_e}{\sqrt{2[E - V(N_e; P_e)]}}, \quad (26a)$$

$$\bar{N} = \frac{2}{\lambda} \int_{N_{min}}^{N_{max}} \frac{N_e dN_e}{\sqrt{2[E - V(N_e; P_e)]}}, \quad (26b)$$

where N_{min} and N_{max} are minimum and maximum levels of $N_e(x)$, respectively, and are derived from $V(N_{min}) = V(N_{max}) = E$ ($0 < N_{min} < \bar{N} < N_{max}$). Equations 26a and 26b give the relationship among P_e , λ , and \bar{N} , where \bar{N} is straightforwardly derived from the initial condition of (u, v) . For Model II (Equation 3),

$$V(N_e; P_e) = \frac{D_v - D_u a_1 P_e}{D_u D_v} \left(N_e^3 - \frac{3 D_v a_2}{2 P_e} N_e^2 \right), \quad (27)$$

and E can range between $E_* < E < 0$ for $N_e(x)$ to be a periodic solution. Here $E_* = -\{[(D_v - D_u)/D_u D_v][(D_v a_1 a_2^3)/(6 P_e^2)]\}$. As E becomes smaller ($E \rightarrow E_*$), the period λ converges to λ_{min} , which is the shortest

wavelength in the periodic solutions. As E becomes larger ($E \rightarrow 0$), the period λ diverges. The solution of $N_e(x)$ at $E = 0$ corresponds to the separatrix of Equation 6b, indicating an infinite period ($\lambda \rightarrow \infty$). The explicit form of $N_e(x)$ for $E = 0$ can be obtained by

$$N_e(x) = \frac{3D_v a_2}{2P_e} \operatorname{sech}^2 \left[\frac{1}{2} \sqrt{\frac{D_v - D_u}{D_u D_v}} a_1 a_2 (x - x_p) \right], \quad (28)$$

which has the sole peak at $x = x_p$ and decays to zero as $x \rightarrow \pm\infty$. For a sufficiently large system, Equation 28 is a good approximation of the solution for $-L/2 < x < L/2$. Equations 28 and 7 lead to Equations 8a and 8b, and 9a–9c.

Solution of Equations 11a and 11b. If there is nontrivial $(n_\mu(x), p_\mu(x))$ that satisfies Equations 11a and 11b for μ with a positive real part, the solution is unstable. Note that $(n_{\mu_0}, p_{\mu_0}) = (n_0 \operatorname{sech}^2(bx), -n_0 P_e / N_0)$ satisfies Equations 11a and 11b for $\mu = 0$ under periodic boundary conditions. Here n_0 is an arbitrary factor, originated from the linearity of equations, and we can set $n_0 = 1$. For μ with an absolute value near zero, we can obtain (n_μ, p_μ) by the expansion from (n_{μ_0}, p_{μ_0}) with regard to μ . To do this, we take $n_\mu = n_{\mu_0} + \mu n_{\mu_1} + \dots$ and $p_\mu = p_{\mu_0} + \mu p_{\mu_1} + \dots$. In the first order of the expansion, (n_{μ_1}, p_{μ_1}) obeys the following equations:

$$\frac{d^2 p_{\mu_1}}{dx^2} = \operatorname{sech}^2(bx), \quad (29a)$$

$$\begin{aligned} \frac{d^2 n_{\mu_1}}{dx^2} &= 4b^2 [1 - 3\operatorname{sech}^2(bx)] n_{\mu_1} - \frac{6b^2 N_0}{P_e} \operatorname{sech}^4(bx) p_{\mu_1} \\ &+ \frac{D_u + D_v}{D_u D_v} \operatorname{sech}^2(bx) + \frac{1}{D_u D_v} \frac{P_e}{N_0}. \end{aligned} \quad (29b)$$

Thus, p_{μ_1} is immediately derived from Equation 29a as:

$$p_{\mu_1}(x) = -\frac{P_e}{N_0} + \frac{\mu}{b^2} \{ \log[\cosh(bx)] + C_1 x + C_2 \}, \quad (30)$$

where C_1 and C_2 are integral constants. We can obtain n_{μ_1} by solving Equation 29b with substitution of p_{μ_1} . C_2 is determined by the mathematical condition that n_{μ_1} should be orthogonal to n_{μ_0} . In practice, C_2 has little influence on (n_{μ_1}, p_{μ_1}) , and we set $C_2 = 0$ in the analysis.

Derivation of v_p from Equations 19a and 19b. The linearized approximations of Equations 19a and 19b are given as follows:

$$2v_p N_0 \tanh(bz) \operatorname{sech}^2(bz) = \frac{\partial^2 p_\varepsilon(z)}{\partial z^2}, \quad (31a)$$

$$\begin{aligned} 0 &= (D_v + D_u) [2v_p N_0 \tanh(bz) \operatorname{sech}^2(bz)] \\ &- D_u D_v \frac{\partial^2 n_\varepsilon(z)}{\partial z^2} + (D_v - D_u) [h_N(z) n_\varepsilon(z) + h_P(z) p_\varepsilon(z) + h_a(z) \varepsilon a_2^*(x)]. \end{aligned} \quad (31b)$$

where $h_N(z) = \partial f^*(N_e(z), P_e a_2) / \partial N$, $h_P(z) = \partial f^*(N_e(z), P_e a_2) / \partial P$, $h_a(z) = \partial f^*(N_e(z), P_e a_2) / \partial a_2^*$. Because t is no longer a variable, we set $t = 0$ without loss of generality and replace z with x in the following analysis. Equation 31a under the periodic boundary condition leads to p_ε as follows:

$$p_\varepsilon(x) = -v_p \frac{N_0}{b} \left[\tanh(bx) - \frac{2}{L} x + C_3 \right], \quad (32)$$

where C_3 is an integral constant. By substituting Equation 32 into Equation 31b, we obtain the following:

References

- Chung CY, Funamoto S, Firtel RA (2001) Signaling pathways controlling cell polarity and chemotaxis. *Trends Biochem Sci* 26: 557–566.
- Iijima M, Huang YE, Devreotes P (2002) Temporal and spatial regulation of chemotaxis. *Dev Cell* 3: 469–478.
- Comer FL, Parent CA (2002) PI 3-kinases and PTEN: How opposites chemoattract. *Cell* 109: 541–544.
- Ridley AJ, Schwartz MA, Burridge K, Firtel RA, Ginsberg MH, et al. (2003) Cell migration: Integrating signals from front to back. *Science* 302: 1704–1709.
- Affolter M, Weijer CJ (2005) Signaling to cytoskeletal dynamics during chemotaxis. *Dev Cell* 9: 19–34.
- Parent CA, Devreotes PN (1999) A cell's sense of direction. *Science* 284: 765–770.
- Firtel RA, Meili R (2000) *Dictyostelium*: A model for regulated cell movement during morphogenesis. *Curr Opin Genet Dev* 10: 421–427.

$$\frac{d^2 n_\varepsilon}{dx^2} = 4b^2 [1 - 3\operatorname{sech}^2(bx)] n_\varepsilon + v_p b N_0 G_n(x) + \varepsilon G_a(x), \quad (33)$$

where $G_n(x)$ and $G_a(x)$ are defined by:

$$\begin{aligned} G_n(x) &= \frac{2(D_u + D_v)}{D_u D_v} \tanh(bx) \operatorname{sech}^2(bx) \\ &+ \frac{6N_0}{P_e} \operatorname{sech}^4(bx) \left[\tanh(bx) - \frac{2}{L} x + C_3 \right], \end{aligned} \quad (34a)$$

$$G_a(x) = \frac{4b^2 N_0}{a_2} \operatorname{sech}^2(bx) a_\varepsilon(x). \quad (34b)$$

By solving Equation 33, we obtain n_ε :

$$\begin{aligned} n_\varepsilon(x) &= W_2(x) \int W_1(x) [v_p b N_0 G_n(x) + \varepsilon G_a(x)] dx \\ &- W_1(x) \int W_2(x) [v_p b N_0 G_n(x) + \varepsilon G_a(x)] dx, \end{aligned} \quad (35)$$

where $W_1(x)$ and $W_2(x)$ are defined by

$$W_1(x) = -2 \tanh(bx) \operatorname{sech}^2(bx), \quad (36a)$$

$$W_2(x) = \frac{-1}{16b} \{ 2 \cosh^2(bx) + 5[1 - 3 \operatorname{sech}^2(bx)] + 15bx \tanh(bx) \operatorname{sech}^2(bx) \}. \quad (36b)$$

Considering the periodic boundary condition for $n_\varepsilon(x)$, we obtain the following equation for sufficiently large L (solvable condition):

$$n_\varepsilon\left(\frac{L}{2}\right) - n_\varepsilon\left(-\frac{L}{2}\right) = W_2\left(\frac{L}{2}\right) \int_{-L/2}^{L/2} W_1(x) [v_p b N_0 G_n(x) + \varepsilon G_a(x)] dx = 0. \quad (37)$$

This leads to the velocity of the peak:

$$v_p = -\frac{\int_{-L/2}^{L/2} W_1(x) \varepsilon G_a(x) dx}{b N_0 Z}, \quad (38)$$

where Z is given as follows:

$$Z = \int_{-L/2}^{L/2} W_1(x) G_n(x) dx = -\frac{64}{15} b \left[\frac{D_v + D_u}{D_v - D_u} \frac{1}{a_1 a_2} + \frac{L^2 \bar{N}^2}{6 D_v a_2} \left(\frac{3}{7} - \frac{1}{bL} \right) \right]. \quad (39)$$

Acknowledgments

We thank Yu-ichi Ozaki, Satoru Sasagawa, Kazuhiro Fujita, and Hidetoshi Urakubo for valuable discussions. We are also grateful to Yuya Terashima and Kouji Matsushima for important comments about the chemotaxis of neutrophils.

Author contributions. MO, SI, CC, KK, AM, and SK conceived and designed the experiments. MO performed the experiments. MO and SI analyzed the data. MO, SI, CC, KK, AM, and SK wrote the paper.

Funding. This work was supported by a grant-in-aid for scientific research from the Ministry of Education, Culture, Sports, Science, and Technology of Japan.

Competing interests. The authors have declared that no competing interests exist.

- Gillitzer R, Goebeler M (2001) Chemokines in cutaneous wound healing. *J Leukoc Biol* 69: 513–521.
- Carlos TM (2001) Leukocyte recruitment at sites of tumor: Dissonant orchestration. *J Leukoc Biol* 70: 171–184.
- Xu J, Wang F, Van Keymeulen A, Herzmark P, Straight A, et al. (2003) Divergent signals and cytoskeletal assemblies regulate self-organizing polarity in neutrophils. *Cell* 114: 201–214.
- Foxman EF, Campbell JJ, Butcher EC (1997) Multistep navigation and the combinatorial control of leukocyte chemotaxis. *J Cell Biol* 139: 1349–1360.
- Devreotes P, Janetopoulos C (2003) Eukaryotic chemotaxis: Distinctions between directional sensing and polarization. *J Biol Chem* 278: 20445–20448.
- Li Z, Hannigan M, Mo Z, Liu B, Lu W, et al. (2003) Directional sensing requires G beta gamma-mediated PAK1 and PIX alpha-dependent activation of Cdc42. *Cell* 114: 215–227.

14. Li Z, Dong X, Wang Z, Liu W, Deng N, et al. (2005) Regulation of PTEN by Rho small GTPases. *Nat Cell Biol* 7: 399–404.
15. Ridley AJ (2001) Rho GTPases and cell migration. *J Cell Sci* 114: 2713–2722.
16. Etienne-Manneville S, Hall A (2002) Rho GTPases in cell biology. *Nature* 420: 629–635.
17. Meili R, Firtel RA (2003) Two poles and a compass. *Cell* 114: 153–156.
18. Ma L, Janetopoulos C, Yang L, Devreotes PN, Iglesias PA (2004) Two complementary, local excitation, global inhibition mechanisms acting in parallel can explain the chemoattractant-induced regulation of PI(3,4,5)P₃ response in *Dictyostelium* cells. *Biophys J* 87: 3764–3774.
19. Levchenko A, Iglesias PA (2002) Models of eukaryotic gradient sensing: Application to chemotaxis of amoebae and neutrophils. *Biophys J* 82: 50–63.
20. Postma M, Van Haastert PJ (2001) A diffusion–translocation model for gradient sensing by chemotactic cells. *Biophys J* 81: 1314–1323.
21. Skupsky R, Losert W, Nossal RJ (2005) Distinguishing modes of eukaryotic gradient sensing. *Biophys J* 89: 2806–2823.
22. Narang A, Subramanian KK, Lauffenburger DA (2001) A mathematical model for chemoattractant gradient sensing based on receptor-regulated membrane phospholipid signaling dynamics. *Ann Biomed Eng* 29: 677–691.
23. Subramanian KK, Narang A (2004) A mechanistic model for eukaryotic gradient sensing: Spontaneous and induced phosphoinositide polarization. *J Theor Biol* 231: 49–67.
24. Meinhardt H (1999) Orientation of chemotactic cells and growth cones: Models and mechanisms. *J Cell Sci* 112: 2867–2874.
25. Sakumura Y, Tsukada Y, Yamamoto N, Ishii S (2005) A molecular model for axon guidance based on cross talk between Rho GTPases. *Biophys J* 89: 812–822.
26. Kaibuchi K, Kuroda S, Amano M (1999) Regulation of the cytoskeleton and cell adhesion by the Rho family GTPases in mammalian cells. *Annu Rev Biochem* 68: 459–486.
27. Nobes CD, Hall A (1995) Rho, Rac, and Cdc42 GTPases regulate the assembly of multimolecular focal complexes associated with actin stress fibers, lamellipodia, and filopodia. *Cell* 81: 53–62.
28. Lim L, Manser E, Leung T, Hall C (1996) Regulation of phosphorylation pathways by p21 GTPases. The p21 Ras-related Rho subfamily and its role in phosphorylation signalling pathways. *Eur J Biochem* 242: 171–185.
29. Giniger E (2002) How do Rho family GTPases direct axon growth and guidance? A proposal relating signaling pathways to growth cone mechanics. *Differentiation* 70: 385–396.
30. Leeuwen FN, Kain HE, Kammen RA, Michiels F, Kranenburg OW, et al. (1997) The guanine nucleotide exchange factor Tiam1 affects neuronal morphology; opposing roles for the small GTPases Rac and Rho. *J Cell Biol* 139: 797–807.
31. Rottner K, Hall A, Small JV (1999) Interplay between Rac and Rho in the control of substrate contact dynamics. *Curr Biol* 9: 640–648.
32. Sander EE, ten Klooster JP, van Delft S, van der Kammen RA, Collard JG (1999) Rac downregulates Rho activity: Reciprocal balance between both GTPases determines cellular morphology and migratory behavior. *J Cell Biol* 147: 1009–1022.
33. Wang HR, Zhang Y, Ozdamar B, Ogunjimi AA, Alexandrova E, et al. (2003) Regulation of cell polarity and protrusion formation by targeting RhoA for degradation. *Science* 302: 1775–1779.
34. Srinivasan S, Wang F, Glavas S, Ott A, Hofmann F, et al. (2003) Rac and Cdc42 play distinct roles in regulating PI(3,4,5)P₃ and polarity during neutrophil chemotaxis. *J Cell Biol* 160: 375–385.
35. Weiner OD, Neilsen PO, Prestwich GD, Kirschner MW, Cantley LC, et al. (2002) A PtdInsP(3)- and Rho GTPase-mediated positive feedback loop regulates neutrophil polarity. *Nat Cell Biol* 4: 509–513.
36. Wang F, Herzmark P, Weiner OD, Srinivasan S, Servant G, et al. (2002) Lipid products of PI(3)Ks maintain persistent cell polarity and directed motility in neutrophils. *Nat Cell Biol* 4: 513–518.
37. Moissoglu K, Slepchenko BM, Meller N, Horwitz AF, Schwartz MA (2006) In vivo dynamics of Rac-membrane interactions. *Mol Biol Cell* 17: 2770–2779.
38. Meinhardt H, Gierer A (2000) Pattern formation by local self-activation and lateral inhibition. *Bioessays* 22: 753–760.
39. Van Keymeulen A, Wong K, Knight ZA, Govaerts C, Hahn KM, et al. (2006) To stabilize neutrophil polarity, PIP₃ and Cdc42 augment RhoA activity at the back as well as signals at the front. *J Cell Biol* 174: 437–445.
40. Zigmond SH, Levitsky HI, Kreel BJ (1981) Cell polarity: An examination of its behavioral expression and its consequences for polymorphonuclear leukocyte chemotaxis. *J Cell Biol* 89: 585–592.
41. Jin T, Zhang N, Long Y, Parent CA, Devreotes PN (2000) Localization of the G protein betagamma complex in living cells during chemotaxis. *Science* 287: 1034–1036.
42. Brock C, Schaefer M, Reusch HP, Czupalla C, Michalke M, et al. (2003) Roles of G beta gamma in membrane recruitment and activation of p110 gamma/p101 phosphoinositide 3-kinase gamma. *J Cell Biol* 160: 89–99.
43. Funamoto S, Meili R, Lee S, Parry L, Firtel RA (2002) Spatial and temporal regulation of 3-phosphoinositides by PI 3-kinase and PTEN mediates chemotaxis. *Cell* 109: 611–623.
44. Huang YE, Iijima M, Parent CA, Funamoto S, Firtel RA, et al. (2003) Receptor-mediated regulation of PI3Ks confines PI(3,4,5)P₃ to the leading edge of chemotaxing cells. *Mol Biol Cell* 14: 1913–1922.
45. Iijima M, Huang YE, Luo HR, Vazquez F, Devreotes PN (2004) Novel mechanism of PTEN regulation by its phosphatidylinositol 4,5-bisphosphate binding motif is critical for chemotaxis. *J Biol Chem* 279: 16606–16613.
46. Iijima M, Devreotes P (2002) Tumor suppressor PTEN mediates sensing of chemoattractant gradients. *Cell* 109: 599–610.
47. Servant G, Weiner OD, Herzmark P, Balla T, Sedat JW, et al. (2000) Polarization of chemoattractant receptor signaling during neutrophil chemotaxis. *Science* 287: 1037–1040.
48. Ishihara S, Otsuji M, Mochizuki A (2007) Transient and steady state of mass-conserved reaction–diffusion systems. *Phys Rev E* 75: 015203.
49. Kondo S (2002) The reaction-diffusion system: a mechanism for autonomous pattern formation in the animal skin. *Genes Cells* 7: 535–541.
50. Murray JD (2003) *Mathematical biology II: Spatial models and biomedical applications*. New York: Springer-Verlag, 736 p.
51. Iron D, Ward MJ, Wei J (2001) The stability of spike solutions to the one-dimensional Gierer–Meinhardt model. *Physica D* 150: 25–62.
52. Munro EM (2006) PAR proteins and the cytoskeleton: A marriage of equals. *Curr Opin Cell Biol* 18: 86–94.
53. Parent CA, Blacklock BJ, Froehlich WM, Murphy DB, Devreotes PN (1998) G protein signaling events are activated at the leading edge of chemotactic cells. *Cell* 95: 81–91.
54. Meili R, Ellsworth C, Lee S, Reddy TB, Ma H, et al. (1999) Chemoattractant-mediated transient activation and membrane localization of Akt/PKB is required for efficient chemotaxis to cAMP in *Dictyostelium*. *EMBO J* 18: 2092–2105.
55. Funamoto S, Milan K, Meili R, Firtel RA (2001) Role of phosphatidylinositol 3' kinase and a downstream pleckstrin homology domain-containing protein in controlling chemotaxis in *Dictyostelium*. *J Cell Biol* 153: 795–810.